

Investigation of ¹³C Isotopic Fractionation of CCH in Two Starless Cores: L1521B and L134N

KOTOMI TANIGUCHI,^{1,2,*} ERIC HERBST,^{1,2} HIROYUKI OZEKI,³ AND MASAO SAITO^{4,5}

¹*Department of Astronomy, University of Virginia, Charlottesville, VA 22904, USA*

²*Department of Chemistry, University of Virginia, Charlottesville, VA 22903, USA*

³*Department of Environmental Science, Faculty of Science, Toho University, Miyama, Funabashi, Chiba 274-8510, Japan*

⁴*National Astronomical Observatory of Japan (NAOJ), Osawa, Mitaka, Tokyo 181-8588, Japan*

⁵*Department of Astronomical Science, School of Physical Science, SOKENDAI (The Graduate University for Advanced Studies), Osawa, Mitaka, Tokyo 181-8588, Japan*

(Received; Revised; Accepted August 27, 2019)

Submitted to ApJ

ABSTRACT

We have carried out observations of CCH and its two ¹³C isotopologues, ¹³CCH and C¹³CH, in the 84 – 88 GHz band toward two starless cores, L1521B and L134N (L183), using the Nobeyama 45 m radio telescope. We have detected C¹³CH with a signal-to-noise (S/N) ratio of 4, whereas no line of ¹³CCH was detected in either the dark clouds. The column densities of the normal species were derived to be $(1.66 \pm 0.18) \times 10^{14} \text{ cm}^{-2}$ and $(7.3 \pm 0.9) \times 10^{13} \text{ cm}^{-2}$ (1σ) in L1521B and L134N, respectively. The column density ratios of $N(\text{C}^{13}\text{CH})/N(^{13}\text{CCH})$ were calculated to be > 1.1 and > 1.4 in L1521B and L134N, respectively. The characteristic that ¹³CCH is less abundant than C¹³CH is likely common for dark clouds. Moreover, we find that the ¹²C/¹³C ratios of CCH are much higher than those of HC₃N in L1521B by more than a factor of 2, as well as in Taurus Molecular Cloud-1 (TMC-1). In L134N, the differences in the ¹²C/¹³C ratios between CCH and HC₃N seem to be smaller than those in L1521B and TMC-1. We discuss the origins of the ¹³C isotopic fractionation of CCH and investigate possible routes that cause the significantly high ¹²C/¹³C ratio of CCH especially in young dark clouds, with the help of chemical simulations. The high ¹²C/¹³C ratios of CCH seem to be caused by reactions between hydrocarbons (e.g., CCH, C₂H₂, *l*, *c*-C₃H) and C⁺.

Keywords: astrochemistry — ISM: individual objects (L1521B, L134N (L183)) — ISM:molecules

1. INTRODUCTION

Exotic unsaturated carbon-chain molecules are one of the crucial constituents of approximately 200 molecules detected in the interstellar medium (ISM) and circumstellar shells. In fact, they account for around 40% of the interstellar molecules. Therefore, it is important for astrochemists to understand carbon-chain chemistry.

These carbon-chain species have long been associated with young starless cores such as Taurus Molecular Cloud-1 (TMC-1; Suzuki et al. 1992; Kaifu et al. 2004). They are formed by gas-phase ion-molecule reactions and neutral-neutral reactions before carbon atoms are converted into CO molecules. Besides the classical carbon-chain chemistry, an ion-molecule chemistry occurring at somewhat higher temperatures, and starting from gaseous methane (CH₄), named warm carbon-chain chemistry (WCCC; Sakai & Yamamoto 2013), was found to occur around low-mass Class 0/I protostars such as L1527. In particular, methane sublimated from dust grains reacts with ionic carbon (C⁺) in the gas phase, which is a trigger of successive carbon-chain formation. It was recently found that formation of cyanopolynes (HC_{2n+1}N, $n = 1, 2, 3, \dots$) occurs in the warm dense gas around high-mass protostellar objects (Taniguchi et al. 2018, 2019b).

Corresponding author: Kotomi Taniguchi
kotomi.taniguchi@gakushuin.ac.jp

* Virginia Initiative on Cosmic Origins Fellow

Current institution: Department of Physics, Faculty of Science, Gakushuin University, Mejiro, Toshima, Tokyo 171-8588, Japan

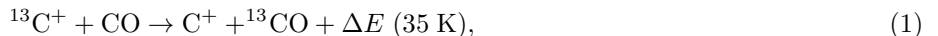
The formation and destruction mechanisms of carbon-chain molecules were investigated mainly by astrochemical simulations (e.g., Suzuki et al. 1992). In these early stages, it was unclear what specific reactions significantly contribute to the formation of carbon-chain species. Another method to investigate the main formation pathways of carbon-chain molecules consists of observations of the ^{13}C isotopic fractionation (e.g., Takano et al. 1998).

The first hint of ^{13}C isotopic fractionation for carbon-chain molecules was found in HC_5N toward TMC-1 using the Nobeyama 45 m radio telescope (Takano et al. 1990). However, signal-to-noise ratios were not high enough to confirm the differences in abundances among its five ^{13}C isotopologues and such studies were left for future work. The confirmation of the ^{13}C isotopic fractionation was achieved for HC_3N in TMC-1 (Takano et al. 1998). Other observations including fractionation studies targeting different carbon-chain molecules were carried out in TMC-1. These species include CCS (Sakai et al. 2007), CCH (Sakai et al. 2010), C_3S and C_4H (Sakai et al. 2013), HC_5N (Taniguchi et al. 2016a), and HC_7N (Burkhardt et al. 2018).

Based on the observations mentioned in the preceding paragraph, some possible main formation pathways of cyanopolyynes were investigated (Takano et al. 1998; Taniguchi et al. 2016a; Burkhardt et al. 2018). In the case of HC_3N , the abundances of H^{13}CCCN and HC^{13}CCN are similar to each other, and HCC^{13}CN is more abundant than the others. From the results, the reaction between C_2H_2 and CN was suggested as the main formation pathway of HC_3N (Takano et al. 1998). On the other hand, there is no significant difference in abundance among the five ^{13}C isotopologues of HC_5N . Reactions between hydrocarbon ions (C_5H_n^+ , $n = 3, 4, 5$) and nitrogen atoms followed by dissociative recombination reactions were found to be the most plausible route to explain the observed ^{13}C isotopic fractionation of HC_5N (Taniguchi et al. 2016a). These proposed reactions were supported by the $^{14}\text{N}/^{15}\text{N}$ ratios of HC_3N and HC_5N (Taniguchi & Saito 2017). In the case of HC_7N , the fractionation results and proposed main formation mechanism are similar to those of HC_5N (Burkhardt et al. 2018).

The main formation mechanisms of HC_3N were investigated in other sources including the L1527 low-mass star-forming core and the G28.28–0.36 high-mass star-forming core (Taniguchi et al. 2016b), as well as two starless cores (L1521B and L134N; Taniguchi et al. 2017). Except for the case of L134N, the reaction between C_2H_2 and CN has been proposed as its main formation mechanism (Taniguchi et al. 2016b, 2017), while the reaction between CCH and HNC could explain the observed ^{13}C isotopic fractionation in L134N (Taniguchi et al. 2017). The proposed main formation pathway of HC_3N in the star-forming cores L1527 and G28.28–0.36 is consistent with model calculations for WCCC (Hassel et al. 2008) and for hot cores (Taniguchi et al. 2019a). The differences among starless cores are probably caused by their different ages; L134N is considered to be more evolved than L1521B and TMC-1 (Taniguchi et al. 2017).

Another interesting feature involving carbon isotopes was the observation that the $^{12}\text{C}/^{13}\text{C}$ ratios of carbon-chain molecules are higher than the elemental ratio in the local interstellar medium (60 – 70; Milam et al. 2005), an effect known as the dilution of the ^{13}C species¹. This dilution is considered to be caused at least in part by the low $^{13}\text{C}^+$ abundance which occurs via the reaction:



a reaction that is efficient especially in low-temperature conditions (Langer et al. 1984). The importance of this reaction stems from the fact that the initial step in the formation of carbon-chain molecules in dark clouds occurs via gas-phase ion-molecule reactions or neutral-neutral reactions with C^+ or C . Hence, the loss of the $^{13}\text{C}^+$ abundance leads to the high $^{12}\text{C}/^{13}\text{C}$ ratios of carbon-chain molecules. However, the different degrees of the dilution of the ^{13}C species among carbon-chain molecules found in TMC-1 cannot be explained only by reaction (1) (Taniguchi et al. 2016a).

In this paper, we report the observations of the $N = 1 - 0$ transition lines of CCH and its two ^{13}C isotopologues in L1521B ($d = 140$ pc) and L134N ($d = 110$ pc) using the Nobeyama 45 m radio telescope. We describe our observations in Section 2. The results and derived parameters with the methods utilized are presented in Section 3. The differential fractionation between the two ^{13}C -containing CCH isotopologues in L1521B and L134N and possible mechanisms causing the heavy dilution of ^{13}C -containing species especially of CCH in dark clouds are discussed with the help of a chemical simulation in Sections 4.1 and 4.2, respectively. Our conclusions are summarized in Section 5.

2. OBSERVATIONS

¹ In this paper, we define the dilution of the ^{13}C species as the $^{12}\text{C}/^{13}\text{C}$ ratios higher than 70, which is the mean $^{12}\text{C}/^{13}\text{C}$ ratio in the local interstellar medium.

The observations were carried out in 2019 January with the Nobeyama 45-m radio telescope (Proposal ID: CG181003, PI: Kotomi Taniguchi, 2018-2019 season). The $N = 1 - 0$ transition lines of CCH and its two ^{13}C isotopologues in the 84 – 88 GHz band were observed simultaneously with the T70 receiver. The beam size and main beam efficiency (η_{mb}) were 19'' and 55%, respectively. The system temperatures were between 170 and 270 K depending on the weather conditions and elevation. We used the SAM45 FX-type digital correlator in the frequency setup whose bandwidth and frequency resolution were 125 MHz and 30.52 kHz, respectively. The frequency resolution corresponds to the velocity resolution of 0.1 km s $^{-1}$ at 86 GHz. We conducted the 2-channel binning in the final spectra, and thus the velocity resolution of the final spectra is 0.2 km s $^{-1}$.

The position-switching mode was employed. The observed positions were $(\alpha_{2000}, \delta_{2000}) = (04^{\text{h}}24^{\text{m}}12^{\text{s}}67, +26^{\circ}36'52''.8)$ and $(15^{\text{h}}54^{\text{m}}12^{\text{s}}72, -02^{\circ}49'47''.4)$ for L1521B and L134N, respectively. The off position for L1521B was set to be $(\Delta\alpha, \Delta\delta) = (+4', +4')$ away from the on-source position, and that for L134N was set at $+3'$ away in the right ascension. The scan pattern was 20 s and 20 s for on-source and off-source positions, respectively. The chopper-wheel calibration method was adopted and hence the absolute calibration error was approximately 10%.

We checked the pointing accuracy by observations of the SiO ($J = 1 - 0$) maser lines from NML Tau at $(\alpha_{2000}, \delta_{2000}) = (03^{\text{h}}53^{\text{m}}28^{\text{s}}86, +11^{\circ}24'22''.4)$ and WX-Ser at $(\alpha_{2000}, \delta_{2000}) = (15^{\text{h}}27^{\text{m}}47^{\text{s}}05, +19^{\circ}33'51''.8)$ during the observations of L1521B and L134N, respectively. The pointing observations were conducted using the H40 receiver every 1.5 hour. The pointing accuracy was within 3''.

3. RESULTS AND ANALYSES

3.1. Results

We conducted the data reduction using Java NEWSTAR, which is the software for data reduction and analyses of the Nobeyama data. The total on-source integration times were 18.75 hr and 23.5 hr for L1521B and L134N, respectively. We fitted the spectra with a Gaussian profile, and the obtained spectral line parameters are summarized in Table 1.

Figure 1 shows the spectra of the normal species of CCH in L1521B and L134N. The black vertical lines indicate the systemic velocities of each source, which are 6.5 km s $^{-1}$ and 2.5 km s $^{-1}$ in L1521B and L134N, respectively. The velocity components of all the transition lines are consistent with the systemic velocities of each source within their errors of 0.2 km s $^{-1}$. Figures 2 and 3 show the spectra of the isotopomers ^{13}CCH (left panels) and C^{13}CH (right panels) in L1521B and L134N, respectively. In either the sources, no line of ^{13}CCH was detected. Two strong transition lines ($J = 3/2 - 1/2, F_1 = 2 - 1, F = 5/2 - 3/2$ and $J = 3/2 - 1/2, F_1 = 2 - 1, F = 3/2 - 1/2$) of C^{13}CH were detected in L1521B and L134N with a signal-to-noise (S/N) ratio of 4. In addition, the weaker transition line ($J = 3/2 - 1/2, F_1 = 1 - 0, F = 1/2 - 1/2$) was tentatively detected with an S/N ratio of 3 in L1521B.

3.2. Analyses

We derived the column densities and excitation temperatures of the normal species with the non-LTE code RADEX (van der Tak et al. 2007). The gas kinetic temperature is assumed to be 10 K, which is a typical value in dark clouds (Hirota et al. 1998). The collision rate coefficients were taken from Spielfiedel et al. (2012). We calculated the parameters using two H_2 densities (n_{H_2}) in each source. The assumed H_2 densities are $1.0 \times 10^5 \text{ cm}^{-3}$ (Hirota et al. 1998) and $5.0 \times 10^4 \text{ cm}^{-3}$ (Hirota et al. 2004) in L1521B, and $1.0 \times 10^5 \text{ cm}^{-3}$ (Hirota et al. 1998) and $2.1 \times 10^4 \text{ cm}^{-3}$ (Dickens et al. 2000) in L134N.

We derived the column densities and excitation temperatures from the intensities of the two weakest hyperfine components by a least-squares method (Sakai et al. 2010)². The derived column densities and excitation temperatures of CCH are $(1.66 \pm 0.18) \times 10^{14} \text{ cm}^{-2}$ and $6.6 \pm 0.7 \text{ K}$ (1σ) for $n_{\text{H}_2} = 1 \times 10^5 \text{ cm}^{-3}$, and $(2.05 \pm 0.2) \times 10^{14} \text{ cm}^{-2}$ and $5.3 \pm 0.6 \text{ K}$ for $n_{\text{H}_2} = 5 \times 10^4 \text{ cm}^{-3}$ in L1521B. For L134N, the column densities and excitation temperatures of CCH were derived to be $(7.3 \pm 0.9) \times 10^{13} \text{ cm}^{-2}$ and $6.4 \pm 0.8 \text{ K}$ for $n_{\text{H}_2} = 1 \times 10^5 \text{ cm}^{-3}$, and $(1.36 \pm 0.17) \times 10^{14} \text{ cm}^{-2}$ and $4.1 \pm 0.5 \text{ K}$ for $n_{\text{H}_2} = 2.1 \times 10^4 \text{ cm}^{-3}$, respectively. Because an excitation temperature of $\sim 6.5 \text{ K}$ is consistent with typical values of carbon-chain molecules in dark clouds (Suzuki et al. 1992) and the critical density of the $N = 1 - 0$ transition of CCH is $1 \times 10^5 \text{ cm}^{-3}$ (Kauffmann et al. 2017), we employ the values obtained with $n_{\text{H}_2} = 1 \times 10^5 \text{ cm}^{-3}$ in the following sections. The excitation temperature of $\sim 6.5 \text{ K}$ is lower than the gas kinetic temperature, but such low excitation temperatures have been derived in prestellar cores (e.g., Padovani et al. 2009).

² The derived excitation temperatures and optical depths of each hyperfine component are summarized in Table 5 in Appendix B.

Table 1. Spectral line parameters of the $N = 1 - 0$ transition of CCH and its two ^{13}C isotopologues in L1521B and L134N

Species	Transition	Frequency ^a (GHz)	$S^{\text{a,b}}$	T_{mb}^{c} (K)	Δv^{c} (km s ⁻¹)	$V_{\text{LSR}}^{\text{d}}$ (km s ⁻¹)	$\int T_{\text{mb}} dv^{\text{c}}$ (K km s ⁻¹)	rms ^e (mK)
L1521B								
CCH	$J = 3/2 - 1/2, F = 1 - 1$	87.284156	0.17	0.588 (9)	0.423 (8)	6.5	0.265 (6)	4.7
	$J = 3/2 - 1/2, F = 2 - 1$	87.316925	1.67	1.165 (12)	0.459 (5)	6.4	0.569 (9)	4.7
	$J = 3/2 - 1/2, F = 1 - 0$	87.328624	0.83	0.843 (10)	0.4223 (6)	6.5	0.379 (7)	4.7
	$J = 1/2 - 1/2, F = 1 - 1$	87.402004	0.83	1.13 (2)	0.405 (9)	6.4	0.485 (14)	5.6
	$J = 1/2 - 1/2, F = 0 - 1$	87.407165	0.33	0.865 (15)	0.408 (8)	6.4	0.375 (10)	5.6
	$J = 1/2 - 1/2, F = 1 - 0$	87.446470	0.17	0.678 (12)	0.405 (8)	6.4	0.292 (8)	5.6
$^{13}\text{CCH}^{\text{f}}$	$J = 3/2 - 1/2, F_1 = 2 - 1, F = 5/2 - 3/2$	84.119329	2.00	< 0.016	< 0.007	3.2
	$J = 3/2 - 1/2, F_1 = 2 - 1, F = 3/2 - 1/2$	84.124143	1.22	< 0.016	< 0.007	3.0
	$J = 3/2 - 1/2, F_1 = 1 - 0, F = 1/2 - 1/2$	84.151352	0.66	< 0.016	< 0.007	2.9
$\text{C}^{13}\text{CH}^{\text{f}}$	$J = 3/2 - 1/2, F_1 = 2 - 1, F = 5/2 - 3/2$	85.229326	2.00	0.026 (13)	0.31 (19)	6.5	0.0084 (7)	3.8
	$J = 3/2 - 1/2, F_1 = 2 - 1, F = 3/2 - 1/2$	85.232792	1.25	0.025 (7)	0.53 (16)	6.5	0.0139 (6)	3.8
	$J = 3/2 - 1/2, F_1 = 1 - 0, F = 1/2 - 1/2$	85.247708	0.65	0.016 (5)	0.7 (3)	6.4	0.0129 (6)	3.5
	$J = 3/2 - 1/2, F_1 = 1 - 0, F = 3/2 - 1/2$	85.256952	1.28	< 0.02	< 0.009	3.6
L134N (L183)								
CCH	$J = 3/2 - 1/2, F = 1 - 1$	87.284156	0.17	0.358 (11)	0.311 (12)	2.6	0.118 (6)	4.8
	$J = 3/2 - 1/2, F = 2 - 1$	87.316925	1.67	0.853 (8)	0.379 (4)	2.5	0.344 (5)	4.8
	$J = 3/2 - 1/2, F = 1 - 0$	87.328624	0.83	0.637 (12)	0.339 (8)	2.5	0.229 (7)	4.8
	$J = 1/2 - 1/2, F = 1 - 1$	87.402004	0.83	0.777 (11)	0.335 (5)	2.5	0.277 (6)	5.4
	$J = 1/2 - 1/2, F = 0 - 1$	87.407165	0.33	0.538 (16)	0.320 (12)	2.5	0.183 (9)	5.4
	$J = 1/2 - 1/2, F = 1 - 0$	87.446470	0.17	0.415 (15)	0.303 (14)	2.5	0.134 (8)	5.4
$^{13}\text{CCH}^{\text{f}}$	$J = 3/2 - 1/2, F_1 = 2 - 1, F = 5/2 - 3/2$	84.119329	2.00	< 0.016	< 0.006	3.1
	$J = 3/2 - 1/2, F_1 = 2 - 1, F = 3/2 - 1/2$	84.124143	1.22	< 0.016	< 0.006	3.1
	$J = 3/2 - 1/2, F_1 = 1 - 0, F = 1/2 - 1/2$	84.151352	0.66	< 0.016	< 0.006	2.9
$\text{C}^{13}\text{CH}^{\text{f}}$	$J = 3/2 - 1/2, F_1 = 2 - 1, F = 5/2 - 3/2$	85.229326	2.00	0.016 (6)	0.7 (3)	2.6	0.011 (6)	3.4
	$J = 3/2 - 1/2, F_1 = 2 - 1, F = 3/2 - 1/2$	85.232792	1.25	0.020 (6)	0.42 (14)	2.5	0.009 (4)	3.3
	$J = 3/2 - 1/2, F_1 = 1 - 0, F = 1/2 - 1/2$	85.247708	0.65	< 0.02	< 0.007	3.6
	$J = 3/2 - 1/2, F_1 = 1 - 0, F = 3/2 - 1/2$	85.256952	1.28	< 0.02	< 0.007	3.7

^a Taken from the Cologne Database for Molecular Spectroscopy, CDMS (Müller et al. 2005).

^b Intrinsic line strength.

^c The numbers in parentheses represent the standard deviation in the Gaussian fit. The errors are written in units of the last significant digit.

^d The errors were 0.2 km s⁻¹, corresponding to the velocity resolution of the final spectra.

^e The rms noises were evaluated in emission-free region in the T_{A}^* scale.

^f The upper limits of the peak intensities correspond to the 3σ limits and those of the integrated intensities were derived from the upper limits of peak intensities assuming that the line widths are equal to the average values of the normal species (0.42 km s⁻¹ and 0.33 km s⁻¹ in L1521B and L134N, respectively).

We derived the column densities of the ^{13}C isotopologues assuming the LTE condition using the following formulae (Taniguchi et al. 2016a):

$$\tau = -\ln \left[1 - \frac{T_{\text{mb}}}{J(T_{\text{ex}}) - J(T_{\text{bg}})} \right], \quad (2)$$

where

$$J(T) = \frac{h\nu}{k} \left\{ \exp\left(\frac{h\nu}{kT}\right) - 1 \right\}^{-1}, \quad (3)$$

and

$$N = \tau \frac{3h\Delta v}{8\pi^3 S} \sqrt{\frac{\pi}{4\ln 2}} Q \frac{1}{\mu^2} \frac{1}{J_{\text{lower}} + 1} \exp\left(\frac{E_{\text{lower}}}{kT_{\text{ex}}}\right) \times \left\{ 1 - \exp\left(-\frac{h\nu}{kT_{\text{ex}}}\right) \right\}^{-1}. \quad (4)$$

In equation (2), T_{mb} is the peak intensity (Table 1) and τ is the optical depth. T_{ex} and T_{bg} are the excitation temperature and the cosmic microwave background temperature (2.73 K), respectively. We assumed that the excitation

Table 2. Column densities and fractional abundances of CCH, column densities of its ^{13}C isotopologues and $^{12}\text{C}/^{13}\text{C}$ ratios in L1521B and L134N

Parameters	L1521B	L134N
$N(\text{CCH}) [\text{cm}^{-2}]^a$	$(1.66 \pm 0.18) \times 10^{14}$	$(7.3 \pm 0.9) \times 10^{13}$
$N(^{13}\text{CCH}) [\text{cm}^{-2}]$	$< 6.2 \times 10^{11}$	$< 5.3 \times 10^{11}$
$N(\text{C}^{13}\text{CH}) [\text{cm}^{-2}]^b$	$(7 \pm 2) \times 10^{11}$	$(7.2 \pm 1.4) \times 10^{11}$
$N(\text{CCH})/N(^{13}\text{CCH})^c$	> 271	> 142
$N(\text{CCH})/N(\text{C}^{13}\text{CH})^c$	252^{+77}_{-48}	101^{+24}_{-16}
$N(\text{H}_2) [\text{cm}^{-2}]$	9.5×10^{21}	1.2×10^{22}
$X(\text{CCH})$	$(1.75 \pm 0.19) \times 10^{-8}$	$(6.1 \pm 0.8) \times 10^{-9}$

NOTE—The errors indicate the standard deviation.

^a The values were derived assuming that n_{H_2} is $1 \times 10^5 \text{ cm}^{-3}$ with the non-LTE method.

^b The errors were calculated from the errors in integrated intensity. We calculated the errors in integrated intensity from the following equation: $\Delta T_{\text{mb}} \times \sqrt{n} \times \Delta v$, where ΔT_{mb} , n , and Δv are rms noise level, the number of channel, and the velocity resolution, respectively.

^c We assumed that the absolute calibration error is cancelled out because all of the lines were observed simultaneously when we derive their errors. This assumption means that the errors of the $^{12}\text{C}/^{13}\text{C}$ ratios would not be affected by the absolute calibration error.

temperatures of the ^{13}C isotopologues of CCH are equal to those of the normal species. We then used the excitation temperatures of $6.6 \pm 0.7 \text{ K}$ and $6.4 \pm 0.8 \text{ K}$ in L1521B and L134N, respectively. $J(T)$ in equation (3) is the effective temperature equivalent to that in the Rayleigh-Jeans law. In equation (4), N denotes the column density, Δv the line width (FWHM), S the line strength, Q the rotational partition function, μ the permanent electric dipole moment, and E_{lower} the energy of the lower rotational energy level. The permanent electric dipole moment is 0.769 Debye for both the ^{13}C isotopologues (Woon 1995). Taking into account the evaluation of the Gaussian fitting, we derived the column densities of C^{13}CH from the line of $J = 3/2 - 1/2, F_1 = 2 - 1, F = 5/2 - 3/2$ in L1521B and the line of $J = 3/2 - 1/2, F_1 = 2 - 1, F = 3/2 - 1/2$ in L134N. In the case of ^{13}CCH , we derived the upper limits of column density from the 3σ upper limits of the peak intensities. We used the average line widths of the normal species: 0.42 km s^{-1} and 0.35 km s^{-1} in L1521B and L134N, respectively. We summarize the column densities derived in each source in Table 2.

Table 2 summarizes the H_2 column density, $N(\text{H}_2)$, at the observed positions. We obtained the $N(\text{H}_2)$ value in L1521B from the fits file of the column density map³. The map was made using the Herschel data (70, 160, 250, 350, and $500 \mu\text{m}$; Palmeirim et al. 2013). We derived the H_2 column density in L134N from the archival data of the 1.2 mm dust continuum emission obtained by the MAMBO bolometer array installed on the IRAM 30 m telescope⁴, using the following formula (Kauffmann et al. 2008):

$$N(\text{H}_2) = 6.69 \times 10^{20} \times F_\nu, \quad (5)$$

where F_ν is the flux intensity in unit of mJy beam^{-1} . The flux intensity is $17.9 \text{ mJy beam}^{-1}$ at the observed position, and the derived H_2 column density is $1.2 \times 10^{22} \text{ cm}^{-2}$ using equation (5). The fractional abundances of CCH, $X(\text{CCH}) = N(\text{CCH})/N(\text{H}_2)$, are calculated at $(1.75 \pm 0.19) \times 10^{-8}$ and $(6.1 \pm 0.8) \times 10^{-9}$ in L1521B and L134N, respectively.

4. DISCUSSION

4.1. ^{13}C Isotopic Fractionation of CCH in L1521B and L134N

³ Taken from http://www.herschel.fr/cea/gouldbelt/en/Phoce/Vie_des_labos/Ast/ast_visu.php?id_ast=66

⁴ Taken from <http://cdsweb.u-strasbg.fr/cgi-bin/qcat?J/A+A/487/993>

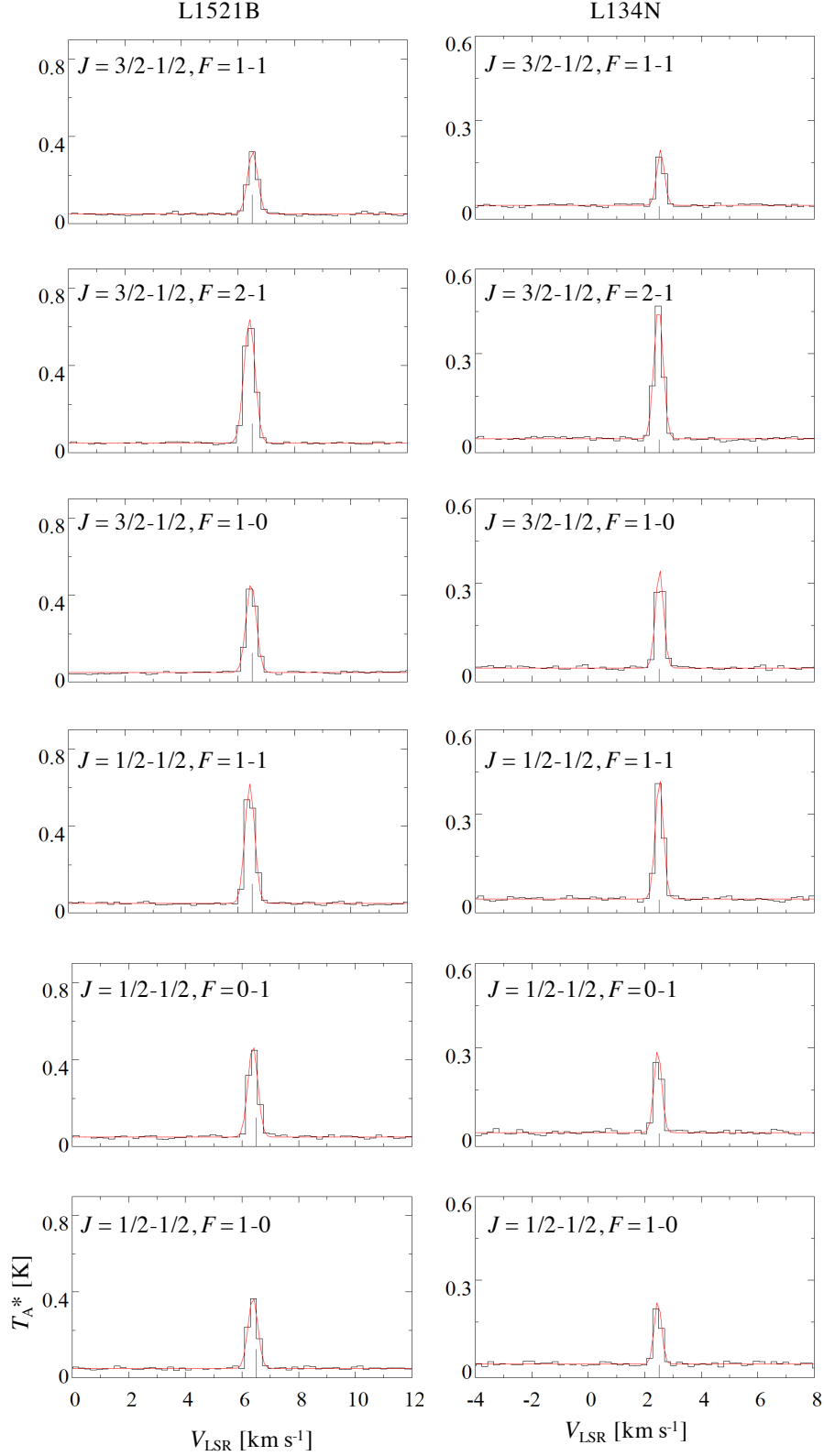


Figure 1. Spectra of the $N = 1 - 0$ transition lines of CCH in L1521B and L134N. The vertical lines indicate the systemic velocities of each source (6.5 km s^{-1} and 2.5 km s^{-1} for L1521B and L134N, respectively). The red curves show the results of the best Gaussian fit.

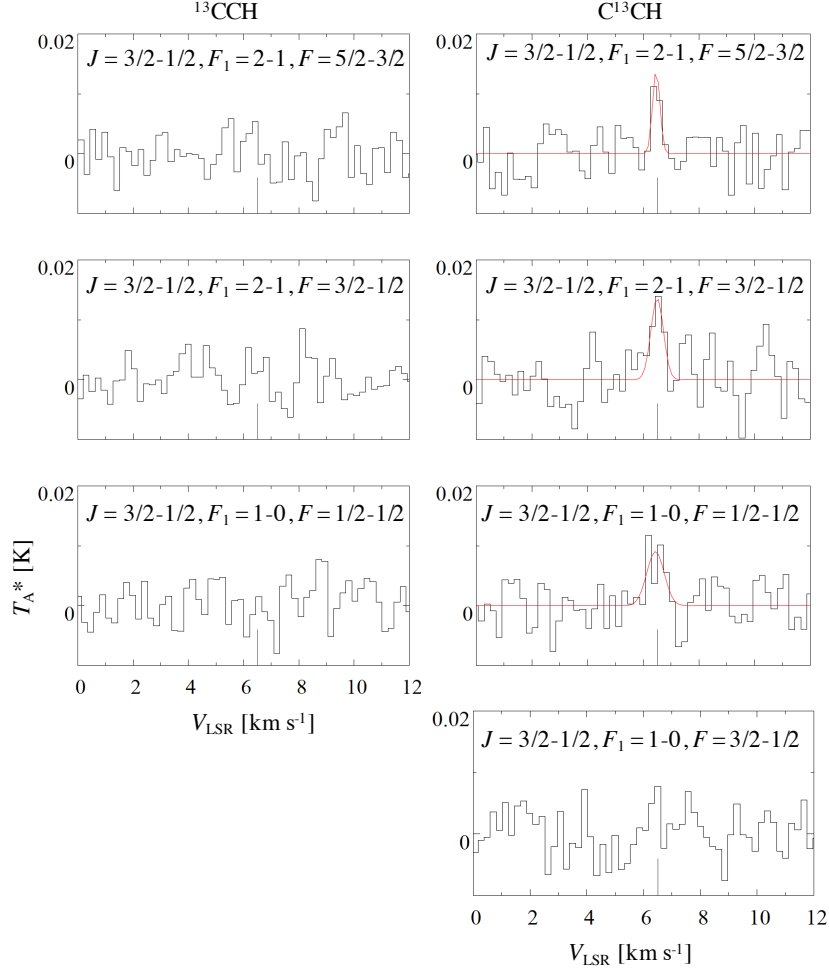
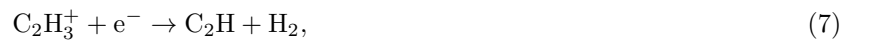
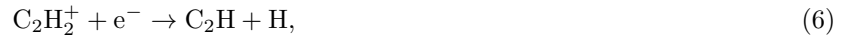


Figure 2. Spectra of the $N = 1 - 0$ transition lines of ^{13}CCH and C^{13}CH in L1521B. The vertical lines indicate the systemic velocity (6.5 km s^{-1}). The red curves show the results of the best Gaussian fit.

In this section, we compare the column densities between the two ^{13}C isotopologues of CCH, namely the fractionation between the two ^{13}C isotopomers, in the observed two starless cores. Because we could not detect ^{13}CCH with an S/N ratio above 3 in the two observed starless cores, we derived lower limits of the $N(\text{C}^{13}\text{CH})/N(^{13}\text{CCH})$ ratio, which are > 1.1 and > 1.4 in L1521B and L134N, respectively⁵. In both sources, the ^{13}CCH isotopomer is less abundant than the C^{13}CH isotopomer. This result is the same as found for TMC-1 and L1527 by Sakai et al. (2010), where the $\text{C}^{13}\text{CH}/^{13}\text{CCH}$ abundance ratios were derived to be 1.6 ± 0.4 and 1.6 ± 0.1 (3σ) respectively. Based on these results, it may be common that ^{13}CCH tends to be less abundant in starless cores.

Two possible mechanisms causing the ^{13}C isotopomer fractionation in CCH have been proposed: fractionation via the formation pathway (Sakai et al. 2010) and via an isotopomer-exchange reaction (Furuya et al. 2011). Sakai et al. (2010) discussed the formation pathways of CCH that could cause its ^{13}C isotopic fractionation. They considered the following three reactions:



and



⁵ These lower limits have the errors of 0.3, which are derived from the standard deviation of $N(\text{C}^{13}\text{CH})$.

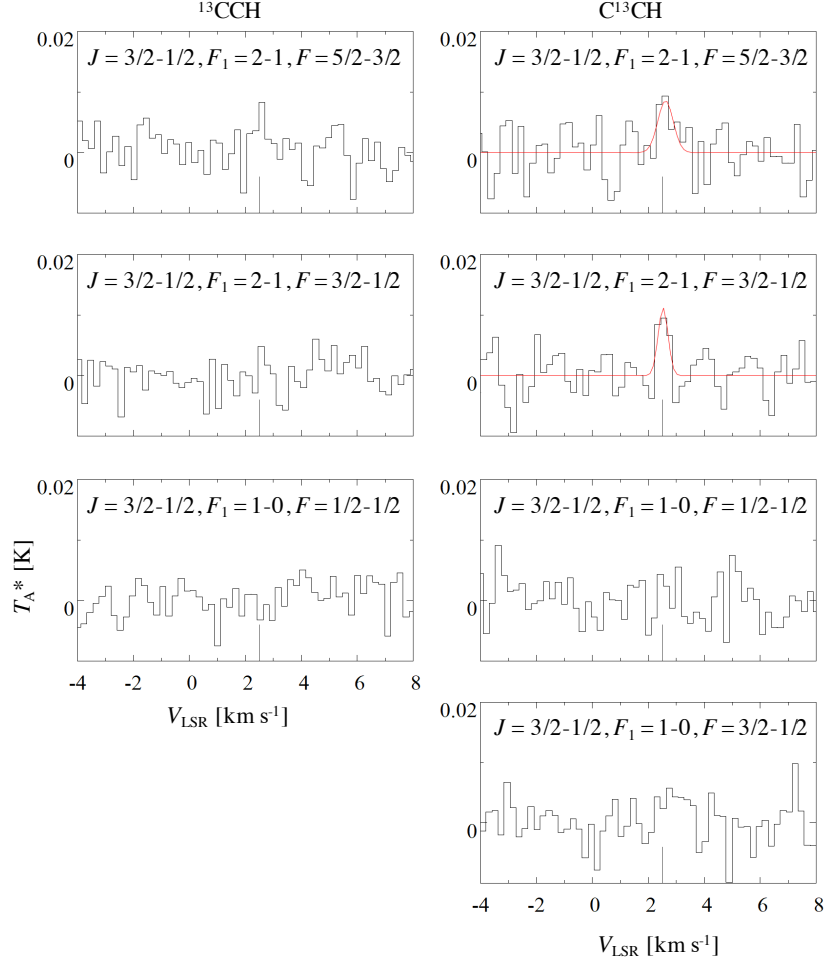


Figure 3. Spectra of the $N = 1 - 0$ transition lines of ^{13}CCH and C^{13}CH in L134N. The vertical lines indicate the systemic velocity (2.5 km s^{-1}). The red curves show the results of the best Gaussian fit.

Among the above three reactions, only reaction (8) is able to cause the ^{13}C isotopic fractionation in CCH, because the two carbon atoms are not clearly equivalent. Hence, Sakai et al. (2010) deduced that the observed differences in the abundances between ^{13}CCH and C^{13}CH would reflect the significant contribution of reaction (8). However, the contributions of each reaction to the overall formation of CCH were not investigated in detail.

We chose to calculate the contributions of each formation pathway of CCH using the astrochemical code Nautilus (Ruaud et al. 2016). Our model calculation and the reaction network utilized are described in Appendix A. Figure 4 shows the results of the model calculation. The upper panel shows the CCH abundance with respect to total hydrogen as a function of time, as well as horizontal lines for the observed abundances in L1521B and L134N. Given the standard level of agreement between calculated and observed abundances in dark clouds, it can be argued that the modeled abundance shows substantial agreement with the observed abundances in both sources over significant periods of time. In addition, estimates of dark cloud ages based on the agreement between observed and calculated abundances for large numbers of molecular species indicate a much tighter constraint on ages centered on the so-called “early time” of $\approx 10^5 \text{ yr}$ (Wakelam et al. 2006).

The lower panel of Figure 4 shows the contribution of each major reaction to the rate of formation of CCH. We exclude reactions which have fractions below 10%. Before 10^3 yr , reaction (6) is the major formation pathway of CCH. The C_2H_2^+ ion has two equivalent carbon atoms, so this reaction cannot explain the differences in abundances between the two ^{13}C isotopologues of CCH. The following reaction has the second highest contribution in this time range:



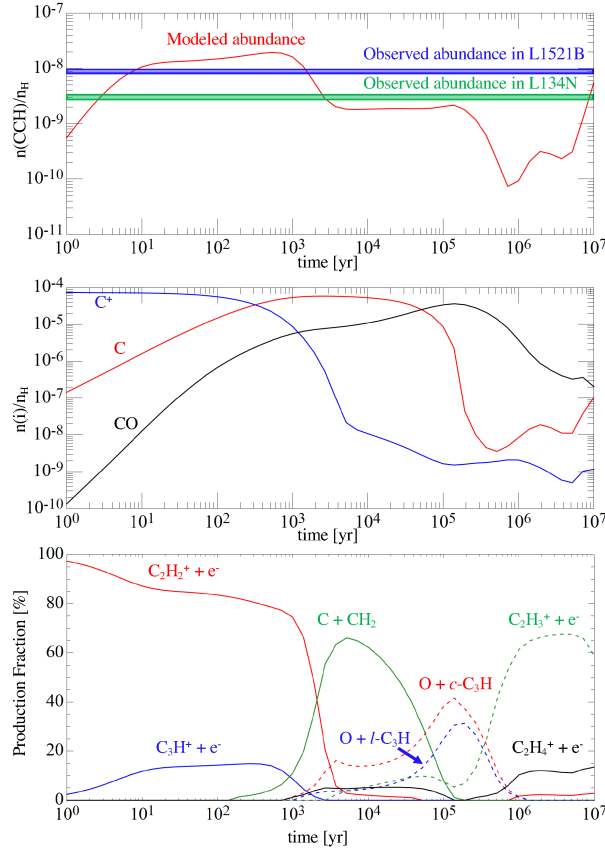


Figure 4. Results of the model calculation. Upper panel; the time dependence of the CCH abundance respect to total hydrogen (red line). The blue and green lines indicate the observed abundances in L1521B and L134N, respectively. Middle panel; the time dependence of the C (red), C^+ (blue), and CO (black) abundances respect to hydrogen. Lower panel; the time dependence of the contribution of each reaction to form CCH.

The three carbon atoms in C_3H^+ are not equivalent, and this can explain the ^{13}C isotopic fractionation, unless scrambling of the carbon atoms occurs efficiently during the electron recombination reaction. However, this reaction contributes a significantly smaller amount to the formation of CCH than reaction (6), and we cannot conclude that reaction (9) significantly contributes to the observable ^{13}C isotopic fractionation of CCH. In addition, although unlikely in such a small system, a scrambling of carbon atoms may occur during ion-molecule reaction that produces C_3H^+ (Taniguchi et al. 2016a). In that case, we would not recognize clear differences in abundances among the ^{13}C isotopologues. The contribution of reaction (9) to the ^{13}C isotopic fractionation of CCH is still unclear.

After 10^3 yr, reaction (8) has the largest contribution to the formation of CCH. As first explained by Sakai et al. (2010), this reaction can result in ^{13}C fractionation because the carbon atoms are not identical. Another way of looking at the problem is that unless the insertion of a carbon atom into the C-H bond occurs at the same rate as its addition to the C of CH_2 and the C atoms can scramble, fractionation will occur. The dominant contribution of reaction (8) extends from somewhat greater than 10^3 yr to almost 10^5 yr, which is a much longer period than the time range when reaction (6) is dominant. Moreover, its range of dominance coincides more closely with the age range determined in multi-molecule fits to abundances in dark clouds (Wakelam et al. 2006). This reaction should therefore contribute to the differences in abundances between ^{13}CCH and C^{13}CH , as mentioned before.

Now consider the case of the isotopomer-exchange reaction:



which is exothermic as written from left-to-right so that the net effect is to increase the abundance of the $^{12}\text{C}^{13}\text{CH}$ isotopomer at the expense of $^{13}\text{C}^{12}\text{CH}$ isotopomer. Furuya et al. (2011) used $1 \times 10^{-10} \text{ cm}^3 \text{ s}^{-1}$ as the rate coefficient

Table 3. The $^{12}\text{C}/^{13}\text{C}$ ratios of CCH and HC_3N in dark clouds

Species	L1521B	L134N	TMC-1
^{13}CCH	> 271	> 142	$> 250^a$
C^{13}CH	252^{+77}_{-48}	101^{+24}_{-16}	$> 170^a$
H^{13}CCCN	117 ± 16^b	61 ± 9^b	79 ± 11^c
HC^{13}CCN	115 ± 16^b	94 ± 26^b	75 ± 10^c
HCC^{13}CN	76 ± 6^b	46 ± 9^b	55 ± 7^c

^a Taken from Sakai et al. (2010).^b Taken from Taniguchi et al. (2017).^c Taken from Takano et al. (1998).

of the forward reaction of the isotopomer-exchange reaction in their calculation. They also applied 8.1 K to the zero-point energy difference of ^{13}CCH and C^{13}CH . The efficiency of this process depends upon a number of factors including whether the exothermicity of 8.1 K is sufficient to cause the difference in observed abundance, whether the abundance of atomic hydrogen is large enough, and whether or not a barrier to reaction exists. The differences in abundances between ^{13}CCH and C^{13}CH can be seen even at the early stages (Figure 3 in Furuya et al. 2011). This isotopomer-exchange reaction appears to be able to explain at least partially the ^{13}C isotopic fractionation in both L1521B and L134N.

In summary, we found that C^{13}CH is more abundant than ^{13}CCH in L1521B and L134N from our observations. This tendency agrees with the previous observations in TMC-1 and L1527 (Sakai et al. 2010). The higher abundance of C^{13}CH compared with ^{13}CCH may indeed be common for dark clouds. Both reaction (8) and the isotopomer-exchange reaction likely contribute to the ^{13}C isotopic fractionation of CCH both in L1521B and L134N.

4.2. The Dilution of the ^{13}C Species in Dark Clouds

4.2.1. Comparisons of the $^{12}\text{C}/^{13}\text{C}$ Ratios between CCH and HC_3N among Dark Clouds

It is interesting to compare the $^{12}\text{C}/^{13}\text{C}$ ratios of CCH and HC_3N among the three dark clouds L1521B, L134N, and TMC-1. Table 3 summarizes the $^{12}\text{C}/^{13}\text{C}$ ratios of CCH and HC_3N in the three dark clouds and Figure 5 shows the comparisons. In the local interstellar medium, the elemental $^{12}\text{C}/^{13}\text{C}$ ratio has been determined to be 60 – 70 (e.g., Milam et al. 2005), which we indicate as the yellow range in Figure 5.

From Figure 5, we find that the dilution of the ^{13}C species in carbon-chain molecules holds for the three observed dark clouds. In addition, the $^{12}\text{C}/^{13}\text{C}$ ratios of CCH tend to be higher than those of HC_3N in all of the dark clouds. It had already been suggested that the degrees of the dilution are different among carbon-chain species in TMC-1 (Taniguchi et al. 2016a). We now can confirm the different degrees of the dilution among the carbon-chain species in the other dark clouds from our observations.

As mentioned in Section 1, the reaction between CCH and HNC was proposed as the main formation pathway of HC_3N in L134N (Taniguchi et al. 2017). In this reaction, the carbon atom in HNC attacks the carbon atom with an unpaired electron in CCH forming HC_3N via HCCCNH (Fukuzawa & Osamura 1997). In that case, we can distinguish all the carbon atoms and trace them during the reaction scheme. We would expect that $\text{HC}_3\text{N}/\text{HC}^{13}\text{CCN}$ is equal to $\text{CCH}/^{13}\text{CCH}$ and $\text{HC}_3\text{N}/\text{H}^{13}\text{CCCN}$ is equal to $\text{CCH}/\text{C}^{13}\text{CH}$. We indicated for the former pair ($\text{HC}^{13}\text{CCN}/\text{HC}_3\text{N}$ and $^{13}\text{CCH}/\text{CCH}$) with red symbols and for the latter pair with blue symbols in Figure 5. The latter pair agree within their 2σ error bars ($\text{CCH}/\text{C}^{13}\text{CH} = 69 - 149$ and $\text{HC}_3\text{N}/\text{H}^{13}\text{CCCN} = 43 - 79$) taking the 2σ errors into consideration. The former pair may marginally lie within the 2σ error bars ($\text{CCH}/^{13}\text{CCH} > 142$ and $\text{HC}_3\text{N}/\text{HC}^{13}\text{CCN} = 42 - 146$), taking the 2σ error into consideration, but we cannot strongly confirm it due to the non-detection of ^{13}CCH . We need data with higher sensitivity in order to reach this conclusion.

In L1521B and TMC-1, the $^{12}\text{C}/^{13}\text{C}$ ratios of CCH are higher than those of HC_3N by more than a factor of 2. The reaction between C_2H_2 and CN was proposed as the main formation pathway of HC_3N in both the dark clouds (Takano et al. 1998; Taniguchi et al. 2017), and the carbon atom which is next to the nitrogen atom in HC_3N should originate from CN, while the other two carbon atoms in HC_3N should come from C_2H_2 (Fukuzawa & Osamura 1997).

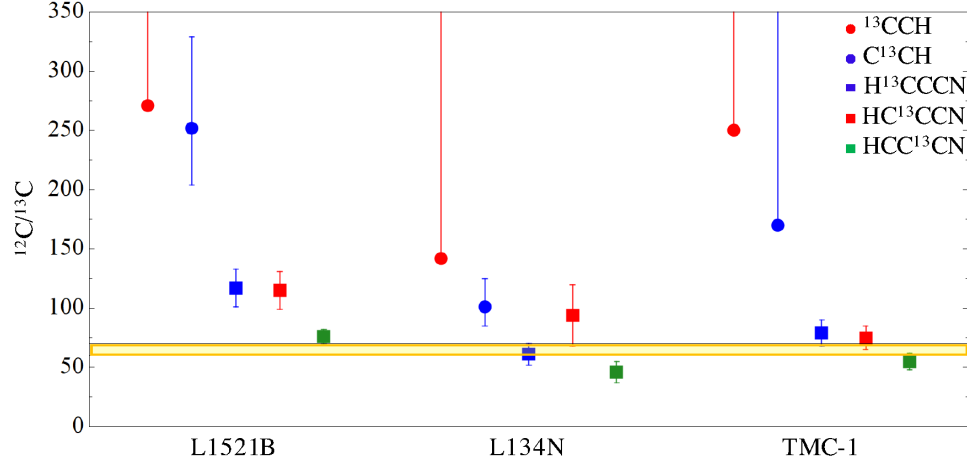


Figure 5. Comparisons of the $^{12}\text{C}/^{13}\text{C}$ ratios of CCH and HC_3N in the three starless cores; L1521B, L134N, and TMC-1. The errors indicate the standard deviation. The yellow range ($^{12}\text{C}/^{13}\text{C} = 60 - 70$) shows the values in the local interstellar medium. The values are the same as Table 3.

Taking these points into consideration, the $^{12}\text{C}/^{13}\text{C}$ ratios of H^{13}CCCN and HC^{13}CCN could reflect those of C_2H_2 . The C_2H_2 molecule is mainly formed by the electron recombination reaction of C_2H_4^+ , which is formed by the reaction between C_2H_2^+ and H_2 (Figure 6). The C_2H_2^+ ion also forms CCH via its electron recombination reaction. Hence, the $^{12}\text{C}/^{13}\text{C}$ ratio of C_2H_2 is expected to be similar to those of CCH, if the $^{12}\text{C}/^{13}\text{C}$ ratios are determined during their bottom-up formation from C^+ and/or C. However, the observational results show discrepancies in the $^{12}\text{C}/^{13}\text{C}$ ratio between CCH and C_2H_2 . This suggests that the different degrees of the dilution of the ^{13}C species are not induced during the carbon-chain growth from C^+ and/or C, but during reactions occurring after their production. In the following subsection, we discuss possible routes which could cause the significantly high $^{12}\text{C}/^{13}\text{C}$ ratios of CCH, especially at a young dark cloud stage.

4.2.2. Possible Routes to Produce the Significantly High $^{12}\text{C}/^{13}\text{C}$ Ratios in CCH

From our model calculation, we uncovered efficient formation and destruction pathways of small hydrocarbons as shown in Figure 6. These pathways were found as we searched for possible routes which cause the high $^{12}\text{C}/^{13}\text{C}$ ratio in CCH.

An important cycle, which seems to be efficient in increasing the $^{12}\text{C}/^{13}\text{C}$ ratio in CCH in stages as early as $t < 10^3$ yr, is highlighted as a red triangle in Figure 6. In this cycle, more than 80% of CCH is destroyed by the reaction with C^+ to form C_3^+ before 10^3 yr. CCH is reformed by the reaction of C_3^+ with H_2 followed by the dissociative recombination of C_3H^+ . If $^{13}\text{C}^+$ is diluted due to reaction (1), the $^{12}\text{C}/^{13}\text{C}$ ratios of CCH will become higher during the cycle because this cycle involves $^{13}\text{C}^+$. Another possible route to produce the high $^{12}\text{C}/^{13}\text{C}$ ratio in CCH involves the following reaction:



The C_3H^+ product once again reacts dissociatively with electrons to form $\text{CCH} + \text{C}$. If the $^{12}\text{C}/^{13}\text{C}$ ratio of C_3H^+ is high, the ratio of CCH also should be high. The following ion-neutral bimolecular reaction could transfer the high $^{12}\text{C}/^{13}\text{C}$ ratio to C_3H^+ :



The high $^{12}\text{C}/^{13}\text{C}$ ratio of C_3H^+ may increase the $^{12}\text{C}/^{13}\text{C}$ ratio of $l, c - \text{C}_3\text{H}_3^+$. However, most electron recombination reactions of $l, c - \text{C}_3\text{H}_3^+$ lead to the formation of $l, c - \text{C}_3\text{H}_2$ and $l, c - \text{C}_3\text{H}$. In that case, the high $^{12}\text{C}/^{13}\text{C}$ ratio of $l, c - \text{C}_3\text{H}_3^+$ will not significantly affect the ratio of C_2H_2 . Therefore, the high $^{12}\text{C}/^{13}\text{C}$ ratio of C_3H^+ will not significantly affect the ratio of C_2H_2 , but produce the high ratio of CCH.

Furuya et al. (2011) plotted the temporal variation of the $^{12}\text{C}^+ / ^{13}\text{C}^+$ ratio. In fact, this ratio takes extremely high value of ≥ 450 around $t \simeq 10^3$ yr with the assumed density of $5 \times 10^4 \text{ cm}^{-3}$ (Figure 1 in Furuya et al. 2011). Therefore, there is a possibility that the above reactions cause the significantly high $^{12}\text{C}/^{13}\text{C}$ ratios in CCH at an early time.

Table 4. Initial elemental abundances with respect to total hydrogen

Element	Abundance
H_2	0.5
He	0.09
C^+	7.3×10^{-5}
N	2.14×10^{-5}
O	1.76×10^{-4}
F	1.8×10^{-8}
Si^+	8×10^{-9}
S^+	8×10^{-8}
Fe^+	3×10^{-9}
Na^+	2×10^{-9}
Mg^+	7×10^{-9}
Cl^+	1×10^{-7}
P^+	2×10^{-10}

NOTE—Taken from the AL model in Acharyya & Herbst (2017).

account, the $^{12}\text{C}/^{13}\text{C}$ ratio of CCH will also become high in the cycle because this cycle involves C^+ . Besides, the reactions of “ $\text{C}_2\text{H}_2 + \text{C}^+$ ” and “ $l, c\text{-C}_3\text{H} + \text{C}^+$ ” can contribute to the high $^{12}\text{C}/^{13}\text{C}$ ratios in CCH.

We are deeply grateful to the staff of the Nobeyama Radio Observatory. The Nobeyama Radio Observatory is a branch of the National Astronomical Observatory of Japan (NAOJ), National Institutes of Natural Science (NINS). K. T. would like to thank the University of Virginia for providing the funds for her postdoctoral fellowship in the Virginia Initiative on Cosmic Origins (VICO) research program. E. H. would like to thank the National Science Foundation for support of his program in astrochemistry.

Facilities: Nobeyama 45 m radio telescope

Software: RADEX (van der Tak et al. 2007), Nautilus (Ruaud et al. 2016)

APPENDIX

A. MODEL CALCULATION

We calculated the abundance of CCH and the contributions of each formation/destruction pathway using the astrochemical code Nautilus (Ruaud et al. 2016). The initial elemental abundances with respect to total hydrogen are taken from (Acharyya & Herbst 2017) as summarized in Table 4. Initially, all of hydrogen is the form in H_2 . The initial form of hydrogen does not affect our discussion. We ran the model calculation including 7646 gas-phase reactions and 498 gas-phase species, mainly taken from the Kinetic Database for Astrochemistry (KIDA)⁶. There are 5323 grain-surface reactions and 431 grain-surface species including suprathreshold species (Shingledecker & Herbst 2018). The surface reactions come mainly from Garrod (2013), with additional data taken from Bergantini et al. (2018) and Hudson & Moore (2018). The self shielding effects of H_2 (Lee et al. 1996), CO (Visser et al. 2009), and N_2 (Li et al. 2013) are included.

⁶ <http://kida.obs.u-bordeaux1.fr>

Table 5. Excitation temperature and optical depth of CCH of each hyperfine component

Line	S	L1521B				L134N			
		$T_{\text{ex}} \text{ (K)}^a$	τ^a	$T_{\text{ex}} \text{ (K)}^b$	τ^b	$T_{\text{ex}} \text{ (K)}^a$	τ^a	$T_{\text{ex}} \text{ (K)}^c$	τ^c
$J = 3/2 - 1/2, F = 1 - 1$	0.17	6.8	0.16	5.4	0.26	6.6	0.10	4.1	0.33
$J = 3/2 - 1/2, F = 2 - 1$	1.67	6.5	0.38	5.1	0.73	6.4	0.27	4.0	1.30
$J = 3/2 - 1/2, F = 1 - 0$	0.83	6.3	0.27	4.9	0.52	6.3	0.20	3.8	0.95
$J = 1/2 - 1/2, F = 1 - 1$	0.83	6.2	0.40	5.0	0.75	6.1	0.27	3.9	1.21
$J = 1/2 - 1/2, F = 0 - 1$	0.33	6.3	0.29	5.0	0.51	6.2	0.17	3.9	0.70
$J = 1/2 - 1/2, F = 1 - 0$	0.17	6.5	0.20	5.3	0.33	6.3	0.13	4.1	0.41

$$^a n_{\text{H}_2} = 1.0 \times 10^5 \text{ cm}^{-3}.$$

$$^b n_{\text{H}_2} = 5.0 \times 10^4 \text{ cm}^{-3}.$$

$$^c n_{\text{H}_2} = 2.1 \times 10^4 \text{ cm}^{-3}.$$

The assumed density, gas temperature, visual extinction (A_V), and cosmic-ray ionization rate (ζ) are $2 \times 10^4 \text{ cm}^{-3}$, 10 K, 10 mag, and $1.3 \times 10^{-17} \text{ s}^{-1}$, respectively. We assume that the dust temperature is equal to the gas temperature. These values are considered to be the typical values for dark clouds (McElroy et al. 2013).

B. EXCITATION TEMPERATURE AND OPTICAL DEPTH OF EACH HYPERFINE COMPONENT

Table 5 summarizes the excitation temperatures and optical depths of CCH of each hyperfine component derived by the RADEX.

REFERENCES

- Acharyya, K., & Herbst, E. 2017, *ApJ*, 850, 105
- Bergantini, A., Góbi, S., Abplanalp, M. J., & Kaiser, R. I. 2018, *ApJ*, 852, 70
- Burkhardt, A. M., Herbst, E., Kalenskii, S. V., et al. 2018, *MNRAS*, 474, 5068
- Dickens, J. E., Irvine, W. M., Snell, R. L., et al. 2000, *ApJ*, 542, 870
- Fukuzawa, K., & Osamura, Y. 1997, *ApJ*, 489, 113
- Furuya, K., Aikawa, Y., Sakai, N., & Yamamoto, S. 2011, *ApJ*, 731, 38
- Garrod, R. T. 2013, *ApJ*, 765, 60
- Hassel, G. E., Herbst, E., & Garrod, R. T. 2008, *ApJ*, 681, 1385
- Hirota, T., Maezawa, H., & Yamamoto, S. 2004, *ApJ*, 617, 399
- Hirota, T., Yamamoto, S., Mikami, H., & Ohishi, M. 1998, *ApJ*, 503, 717
- Hudson, R. L., & Moore, M. H. 2018, *ApJ*, 857, 89
- Kaifu, N., Ohishi, M., Kawaguchi, K., et al. 2004, *PASJ*, 56, 69
- Kauffmann, J., Bertoldi, F., Bourke, T. L., Evans, N. J., II, & Lee, C. W. 2008, *A&A*, 487, 993
- Kauffmann, J., Goldsmith, P. F., Melnick, G., et al. 2017, *A&A*, 605, L5
- Langer, W. D., Graedel, T. E., Frerking, M. A., & Armentrout, P. B. 1984, *ApJ*, 277, 581
- Lee, H.-H., Herbst, E., Pineau des Forets, G., Roueff, E., & Le Boulrot, J. 1996, *A&A*, 311, 690
- Li, X., Heays, A. N., Visser, R., et al. 2013, *A&A*, 555, A14
- McElroy, D., Walsh, C., Markwick, A. J., et al. 2013, *A&A*, 550, A36
- Milam, S. N., Savage, C., Brewster, M. A., Ziurys, L. M., & Wyckoff, S. 2005, *ApJ*, 634, 1126
- Müller, H. S. P., Schlöder, F., Stutzki, J., & Winnewisser, G. 2005, *Journal of Molecular Structure*, 742, 215
- Padovani, M., Walmsley, C. M., Tafalla, M., et al. 2009, *A&A*, 505, 1199
- Palmeirim, P., André, P., Kirk, J., et al. 2013, *A&A*, 550, A38
- Ruaud, M., Wakelam, V., & Hersant, F. 2016, *MNRAS*, 459, 3756
- Sakai, N., Ikeda, M., Morita, M., et al. 2007, *ApJ*, 663, 1174
- Sakai, N., Takano, S., Sakai, T., et al. 2013, *Journal of Physical Chemistry A*, 117, 9831
- Sakai, N., Saruwatari, O., Sakai, T., Takano, S., & Yamamoto, S. 2010, *A&A*, 512, A31
- Sakai, N., & Yamamoto, S. 2013, *Chemical Reviews*, 113, 8981

- Shingledecker, C. N., & Herbst, E. 2018, *Physical Chemistry Chemical Physics (Incorporating Faraday Transactions)*, 20, 5359
- Spielfiedel, A., Feautrier, N., Najjar, F., et al. 2012, *MNRAS*, 421, 1891
- Suzuki, H., Yamamoto, S., Ohishi, M., et al. 1992, *ApJ*, 392, 551
- Takano, S., Masuda, A., Hirahara, Y., et al. 1998, *A&A*, 329, 1156
- Takano, S., Suzuki, H., Ohishi, M., et al. 1990, *ApJL*, 361, L15
- Taniguchi, K., Herbst, E., Caselli, P., et al. 2019a, *arXiv e-prints*, arXiv:1906.11296
- Taniguchi, K., Ozeki, H., & Saito, M. 2017, *ApJ*, 846, 46
- Taniguchi, K., Ozeki, H., Saito, M., et al. 2016a, *ApJ*, 817, 147
- Taniguchi, K., & Saito, M. 2017, *PASJ*, 69, L7
- Taniguchi, K., Saito, M., & Ozeki, H. 2016b, *ApJ*, 830, 106
- Taniguchi, K., Saito, M., Sridharan, T. K., & Minamidani, T. 2018, *ApJ*, 854, 133
- Taniguchi, K., Saito, M., Sridharan, T. K., & Minamidani, T. 2019b, *ApJ*, 872, 154
- van der Tak, F. F. S., Black, J. H., Schöier, F. L., Jansen, D. J., & van Dishoeck, E. F. 2007, *A&A*, 468, 627
- Visser, R., van Dishoeck, E. F., & Black, J. H. 2009, *A&A*, 503, 323
- Wakelam, V., Herbst, E., & Selsis, F. 2006, *A&A*, 451, 551
- Woon, D. E. 1995, *Chemical Physics Letters*, 244, 45